Development and optimization of large-scale integration of 2D material in memristors

Clotilde Ligaud, Lucie Le Van-Jodin, Bruno Reig, Pierre Trousset, Paul Brunet, Michaël Bertucchi, Clémence Hellion, Nicolas Gauthier, Van-Hoan Le, Hanako Okuno, et al.

Development and optimization of large-scale integration of 2D material in memristors.

Clotilde Ligaud[1], Lucie Le Van-Jodin[1], Bruno Reig[1], Pierre Trousset[1], Paul Brunet[1], Michaël Bertucchi[1], Clémence Hellion[1], Nicolas Gauthier[1], Le Van-Hoan[1], Hanako Okuno[2], Djordje Dosenovic[2], Stéphane Cadot[1], Remy Gassilloud[1], Matthieu Jamet[3]

[1] Univ. Grenoble Alpes, CEA, Leti, F-38000 Grenoble, France
[2] Univ. Grenoble Alpes, CEA, IRIG, MEM, F-38000 Grenoble, France
[3] Univ. Grenoble Alpes, CEA, CNRS, Grenoble INP, IRIG, Spintec, F-38000 Grenoble, France

E-mail: lucie.levan-jodin@cea.fr

Received xxxxxx
Accepted for publication xxxxxx
Published xxxxxx

Abstract

Two-dimensional (2D) materials like transition metal dichalcogenides (TMD) have proved to be serious candidates to replace silicon in several technologies with enhanced performances. In this respect, the two remaining challenges are the wafer scale growth of TMDs and their integration into operational devices using clean room compatible processes. In this work, two different CMOS-compatible protocols are developed to compare the resulting performances of MoS_2-based memristors. The quality of MoS_2 at each stage of the process is characterized by Raman spectroscopy and x-ray photoemission spectroscopy. In the first protocol, the structure of MoS_2 is preserved during transfer and patterning processes. However, a polymer layer with a minimum thickness of 3 nm remains at the surface of MoS_2 limiting the electrical switching performances. In the second protocol, the contamination layer is completely removed improving electrical switching performances and reproducibility. Based on physico-chemical and electrical results, the switching mechanism is discussed in terms of conduction through grain boundaries.

Keywords: MoS_2, 2D material, integration, memristor, switching mechanism

1. Introduction

Since the discovery of the unique properties of graphene [1], 2D materials have been holding great promises for the development of high-performance electronic devices. In particular, the intrinsic properties of MoS_2 could allow the development of flexible devices [2], sensors [3], [4], high responsivity (10^4 mA/W) phototransistors [5], non-volatile memory devices [6] , high cut-off frequency RF switches [[7], [8], [9], [10]] or transistors [11], [12].

For memory devices, MoS_2 has been integrated in nanoscale vertical metal-insulator-metal (MIM) structure resulting in high performances devices [13] with low switching voltage, fast switching speed and high ON/OFF current ratio enabling the manufacture of multi-level devices [14], [15] and opening the way to the development of RF switches [13], [16].

However, despite recent promising results, the atomic mechanisms for the formation of On and OFF states in these devices are not yet well understood. Several hypotheses have been put forward. Wang et al. [17], explain the switching behaviour in partially oxidised MoS_2 by the formation of a conductive filament made of sulphur vacancies which is formed or resorbed by the diffusion of oxygen ions. In the devices presented by Yin et al. [18], the MoS_2 was included in

a mixture with graphene-oxide nanosheets. They proposed a switching mechanism based on the formation and dissolution of conductive filaments due to the migration of oxygen ion and their reabsorption from the mixture into an insulating layer appearing at the Al electrode/mixture interface. Most of articles [10], [19], [20] suggest that diffusion of metal ions into sulphur vacancies forms conductive filament. Regarding devices based on MoS_2 nanosheets, Tang et al. [21] explained the electrical switching by the migration of sulphur vacancies only at the edge of the nanosheets. Finally, Zhang et al. [22] justified the switching of the devices by the presence of local phase change. None of these hypotheses has been formally confirmed, moreover, they are not incompatible and several of them, could coexist in the same device.

Memristor performances and our understanding of switching mechanisms are currently limited by the low yield of switching devices, lack of reproducibility and weak endurance after manufacturing [23]. 2D material integration process with CMOS capability is a challenge and still limits the performance of devices for memory as well as for other applications: photoFET [24] or Sensors [25]. Because of their unique structure, 2D materials are particularly sensitive to traditional integration processes in the semiconductor industry [26]. The following points are particularly critical and have been highlighted in recent years: polymer contamination [27], [28], how to manage Van der Waals interfaces [12], [29] or electrical contact [30], [31], [32].

In this study, we developed and optimised a complete process for integrating 2D materials into a fully CMOS-compatible vertical MIM structure in a clean room and over a large area. The preservation of the physico-chemical properties of MoS_2 is checked and optimised along the whole fabrication process. Electrical measurements are performed to study the effect of the fabrication protocol, the top electrode metal and the MoS_2 grain size. Eventually, switching mechanisms are discussed in terms of conduction through grain boundaries.

2. Experimental methods

2.1 MoS_2

Two types of MoS_2 were integrated in devices. MoS_2-A sample corresponds to MoS_2 deposited by Atomic Layer deposition (ALD) onto 8'' Si/SiO_2 wafer with $Mo(NMe_2)_4$ and 1,2-ethanedithiol as precursors around 100°C. An annealing treatment at 900°C under inert atmosphere is performed to improve the crystallinity. The detailed method is given in Ref [33]. MoS_2B sample is provided by 2D semiconductor. The deposition was done by CVD onto 2'' sapphire substrate. MoS_2-B sample correspond to one monolayer [34].

2.2 Characterization

X-ray photoelectron spectrometry (XPS) measurements were performed with a PHI 5000 VersaProbe II photoelectron spectrometer at the Nanocharacterization Platform (PFNC) of the Minatec Campus in Grenoble (France). The samples were inserted in ultrahigh vacuum and excited by a 200 µm diameter monochromatic Al-Kα (hν = 1486.6 eV) X-ray light source. The source analyser angle is 45° and remains unchanged during the XPS data acquisition, where the photoelectron take-off angle (sample-analyser angle) also fixed at 45° does not vary either. The overall energy resolution (taking into account both the spectrometer and X-ray bandwidths) is 0.6 eV for Core Level spectra and we set the C 1s peak from the adventitious carbon to 284.8 eV for calibration of the binding energy scale. Data correction and peak deconvolution were performed with the CasaXPS software, and we used the sensitivity factors provided by the instrument to perform the relative quantification of the elements.

Atomic force microscopy (AFM) measurements were performed on a Dimension ICON (Bruker) in PeakForce Tapping mode using a "ScanAsyst Air" cantilever (nominal stiffness: 40 N/m; tip radius of curvature: 5 nm; and approach-withdrawal frequency: 2 kHz).

Raman spectroscopy spectra were obtained using a Renishaw inVia Reflex spectrometer with a 532 nm laser diode excitation source in a range of 100-1000 cm^{-1}. To determine width and peak positions, the curves were fitted using the same method as in Mignuzzi et al [35].

Cross-section specimen for transmission electron microscopy (TEM) were prepared using a Zeiss crossbeam 750 FIBSEM.

Scanning Transmission electron microscopy (STEM) analyses were performed using a Cs-corrected FEI-Titan Themis microscope, operating at 200 kV and allowing high angle annular dark field (HAADF) imaging and subsequent energy-dispersive X-ray (EDX) chemical mapping.

Electrical measurements were performed in ambient conditions under two tungsten tips using a Keysight B1500A Semiconductor Analyser with: a B1517A High Resolution Source Measurement Unit. Each measurement involves applying a voltage sweep between the two tips and measuring the current. To control the formation of the conductive filament, a compliance current was set during the tuning operation, the value of which was approximately 10^{-5} A.

2.3 Devices fabrication

The goal of the integration process is to develop vertical cross memory devices as illustrated in figure 1-a and d. A first protocol called protocol I was used to manufacture the first devices. It was then optimized to protocol II for devices with improved performances.

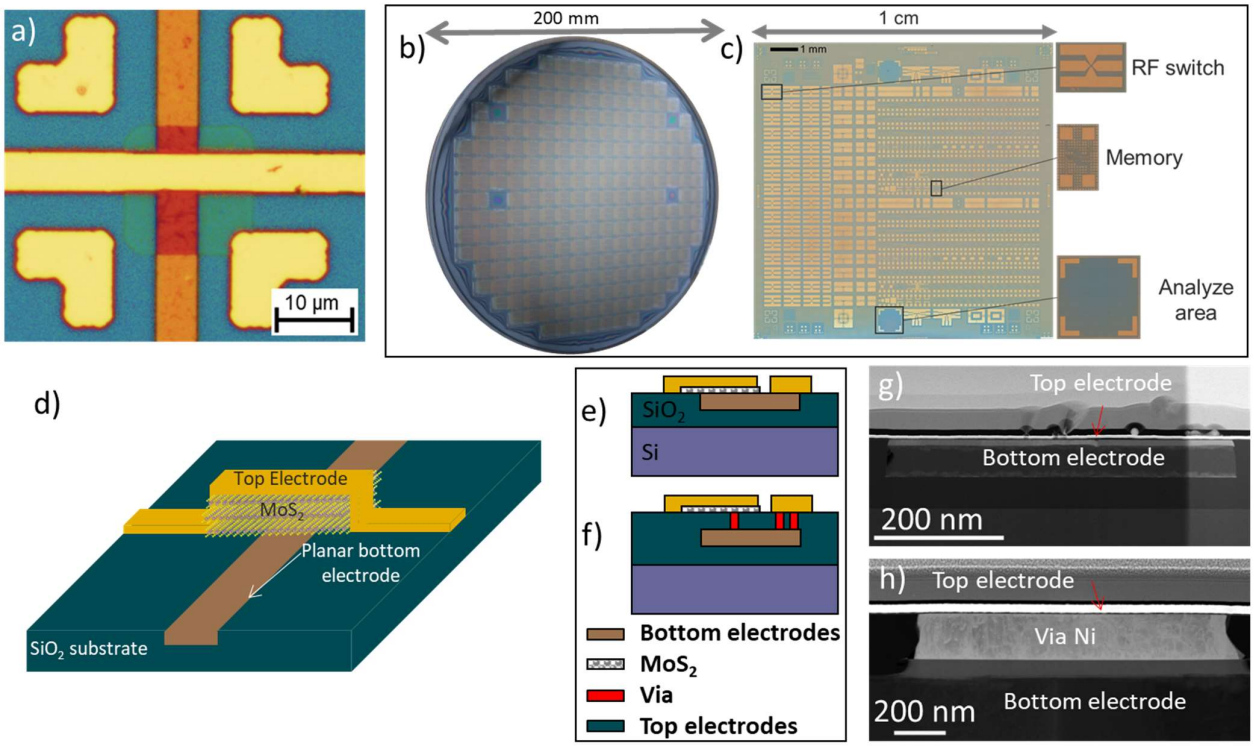

Figure 1: Integration process: Picture of the 200 mm wafer including the back electrodes (b) with about 250 dice, Optical image of one die with some detailed devices (c) memristor devices schematic (d) and optical image (a) and schematic cross-section representation of the 2 architectures of bottom electrode without (e)and with via (f) cross-section TEM image of architecture without (g) and with via (h).

2.3.1 Bottom electrodes

Planar bottom electrodes are manufactured on 200 mm wafers in clean room using standard microelectronic processes. Using planar electrodes avoids the presence of defects related to the MoS_2 transfer onto 3D electrodes where step edges might break the film continuity. Each wafer contains 250 dice with various designs as presented in Figure 1-a. Several devices are patterned on each chip but only memories (cross devices) are used in this work (Figure 1-c, d).

Two types of bottom electrodes are considered. In protocol I, they consist of the following stack: Ti(10 nm)/AlCu(440 nm)/Ti(10 nm) and TiN (100 nm) on top (Figure 1-e and g). In protocol II nickel via were integrated on top of the TiN electrode (Figure 1-f and h). The typical size of the active part of the cross-devices without and with via is about 25 µm² and 1 µm² respectively. For the rest of the procedure, the 8'' wafer is cut in smaller dice of 9 cm².

The following steps are summarized for each protocol in Table I.

Table I : Detailed process integration steps for protocol I and protocol II.

	Potocol I	**Protocol II**
MoS_2 transfer	Wet transfer (polymer assist)	Wet transfer (polymer metal assist)
MoS_2 patterning	Photolithography	Deep UV lithography
	ICP	IBE
Top electrodes deposition and patterning	Photolithography	Deep UV lithography with double PMMA layer
	EBPVD	EBPVD
	Lift-off	Optimized lift-off

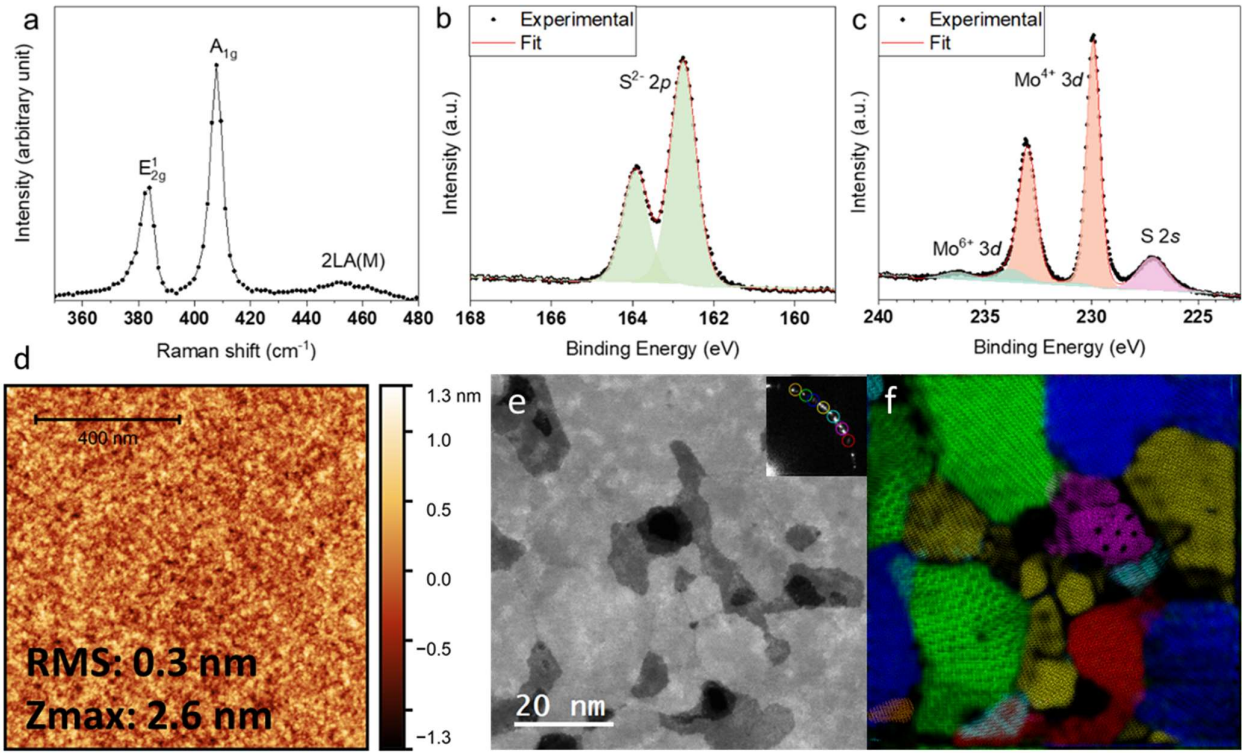

Figure 2 : Physico-chemical characterization of MoS_2-A. Raman spectroscopy spectrum (a). S 2p (b) and Mo 3d (c) XPS spectra. AFM image (d). In-plane view of three monolayers of MoS_2 obtained by scanning transmission electron microscopy (STEM) (f), high resolution image with fast Fourier transform in the inset showing the MoS_2 crystalline diffraction pattern and (g): corresponding spatial distribution of grains in false colours.

2.3.2 Transfer and patterning of MoS_2

The MoS_2 transfer is performed using the classical wet transfer method in protocol I. A solution of liquid polymethyl methacrylate (PMMA) is spin-coated on the surface of the $MoS_2/SiO_2/Si$ sample and backed at 180°C for 5 min to remove the solvent. The $MoS_2/SiO_2/Si$ sample is then dipped into water to detach the stack MoS_2/PMMA from the Si substrate. The stack is fished with a die of few square centimeters. The sample is dried in air and the PMMA removed by acetone. In protocol II, a thin Au-layer was deposited by evaporation on top of MoS_2 before the wet transfer. For protocol I, MoS_2 is patterned by a standard photolithography step using AZ1512HS as photoresist and AZ developer followed by an inductively coupled plasma (ICP) with CF_4. In protocol II a deep UV lithography is used with PMMA as photoresist., followed by an ion beam etching (IBE) step.

2.3.3 Top electrodes

Finally, top electrodes are deposited by electron beam physical vapor deposition (EBPVD) for, to avoid any MoS_2 damage and patterned by lift off. Three types of electrodes are used for devices without via: Ni 10 nm, Ti-10 nm/Pt 90 nm and Cr-2 nm/Au-98 nm. Ti and Cr are used as adhesive layers on SiO_2. For devices with via, in protocol II, only Au-100 nm are used. The resin and remover used for this process are PMMA and acetone respectively. The effect of an annealing at 300°C under an inert atmosphere of nitrogen and during 2 hours is studied to remove residual organic contamination and improve interfaces.

3 Results and discussion

3.1 MoS_2 characterization

3.1.1 MoS_2-A

Raman spectroscopy was used to check the crystal quality, homogeneity, and number of MoS_2 layers in an area of 7x7 µm² comparable to the size of the active layer in cross devices. First, 49 scans were recorded to control the sample homogeneity. All the spectra superimpose (see Supplementary Figure S1). Figure 1-a exhibits the two MoS_2 characteristic vibration modes E^1_{2g} and A_{1g} at 383.2 and 407.7 cm^{-1} respectively and also the 2LA(M) mode at 452.0 cm^{-1} [36]. The Raman peaks are very narrow, typically 5.4 and 5.3 cm^{-1} for modes E^1_{2g} and A_{1g} respectively. It demonstrates the good crystalline quality of the film [35]. According to Li et al. [37], the gap between the two main peaks changes as a function of the number of layer. A gap of 24.5 cm^{-1} was observed which corresponds to 4 monolayers (ML).

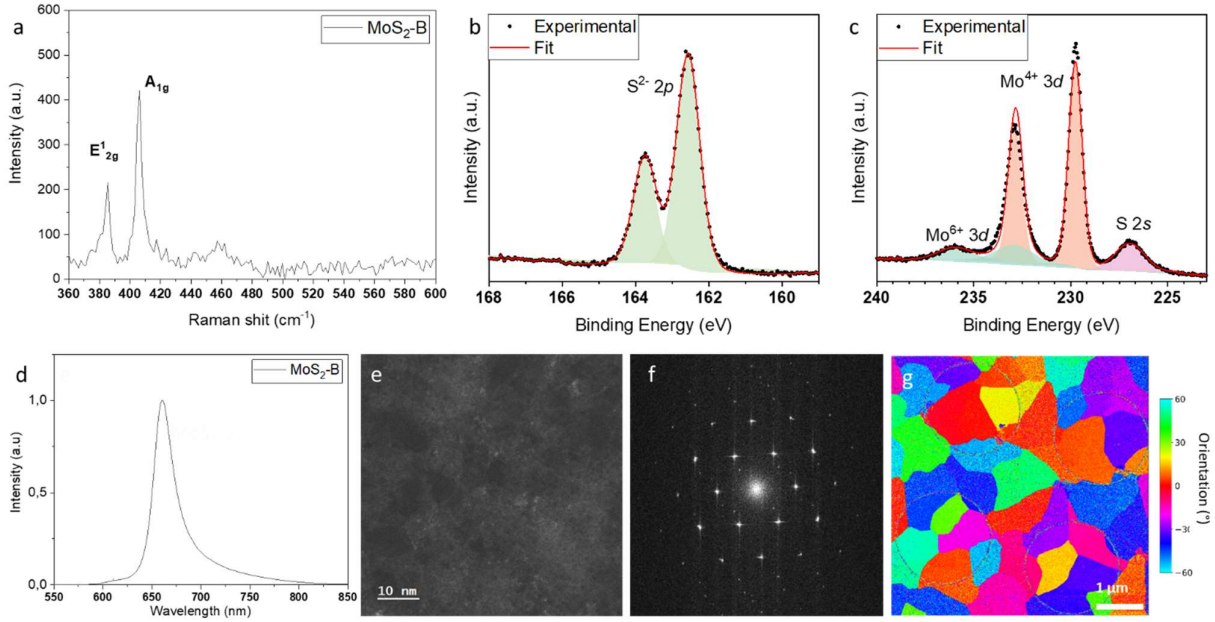

Figure 3: Physico-chemical characterization of MoS_2-B. Raman spectroscopy spectrum (a). S 2p (b) and Mo 3d (c) XPS spectra. photoluminescence spectrum (d), Plane view of three monolayers of MoS_2 by scanning transmission electron microscopy (STEM) (e), high resolution image with fast Fourier transform in the inset showing the MoS_2 crystalline diffraction pattern (f)and spatial distribution of grains in false colors plotted using the 4D-STEM method [42] (g).

Rutherford Backscattering spectroscopy (RBS) and X-ray photoelectron spectrometry (XPS) were performed to study the chemical composition of the material. RBS (Supplementary Figure S2) reveals a slight deficiency in sulphur since S/Mo ratio was determined as 1.76 ± 0.15. This sulphur deficiency is confirmed by XPS quantifying an atomic ratio between Mo 3*d* and S 2*p* orbitals of 1.8. (Supplementary Table 1). Figure 2.-b and c show the high resolution XPS spectra of Mo 3*d* and S 2*p*, respectively including deconvolution curves. The most intense peaks located at 229.9 and 233.0 eV are attributed to the doublet of Mo^{4+} $3d_{5/2}$ and Mo^{4+} $3d_{3/2}$ corresponding to Mo-S bonding, in agreement with the presence of 2H-MoS_2[38]. Another doublet is visible on the spectrum at the following positions: 234 and 236.6 eV corresponding to the doublet of Mo^{6+} $3d_{5/2}$ and Mo^{6+} $3d_{3/2}$[39]. These peaks indicate the presence of Mo-O bonds as a consequence of MoS_2 weak oxidation due to air exposure[40]. In the S 2*p* spectrum, two peaks are observed at 162.7 and 163.9 eV corresponding to the doublet of S^{2-} $2p_{3/2}$ and S^{2-} $2p_{1/2}$ respectively. These peaks are also attributed to Mo-S bonding [41].

Atomic force microscopy (AFM) was used to study the film morphology. A 1x1 µm^2 image is shown in figure-d. The measured root-mean-square (RMS) roughness is as low as 0.3 nm for a surface of 1x1 µm2 and the maximum peak-valley value is 2.6 nm. It shows the very good flatness of MoS_2-A.

Finally, scanning transmission electron microscopy (STEM) was used to probe the atomic structure of MoS_2-A. The images of figure1-e and f demonstrate the polycrystalline character of the film with an average domain size of 10 nm and random crystalline orientation.

3.1.2 MoS_2-B

MoS_2-B was characterized using the same methods. Figure 3-a, exhibits the two MoS_2 characteristic vibration modes E^1_{2g} and A_{1g} at 384.8 and 405.9 cm^{-1} respectively and also the 2LA(M) mode at 440.5 cm^{-1} The Raman peaks are very narrow, typically 5,2 and 4.6 cm^{-1} for E^1_{2g} and A_{1g} respectively. It demonstrates the good crystallinity of the film [35]. The gap between the two main peaks is 18.5 cm^{-1}, according to Li et al. [37] , it corresponds to 1 monolayer.

Figure 3-b and c show the high resolution XPS spectra of Mo 3d and S 2p including the deconvolution curves. By XPS we find an atomic ratio between Mo 3*d* and S 2*p* orbitals equal to 2. The binding energy gap between Mo $3d_{5/2}$ and S $2p_{3/2}$ of MoS_2-B is determined as 67.25 eV which confirms the good stoichiometry [30] of MoS_2. Figure 3-d shows photoluminescence spectra. The intensity and thinness of the lines highlights a typical well-crystallized MoS_2 monolayer. These observations are confirmed by the TEM images (Figure 3 e—g) showing a homogeneous monolayer with a domain size of ~1 µm^2.

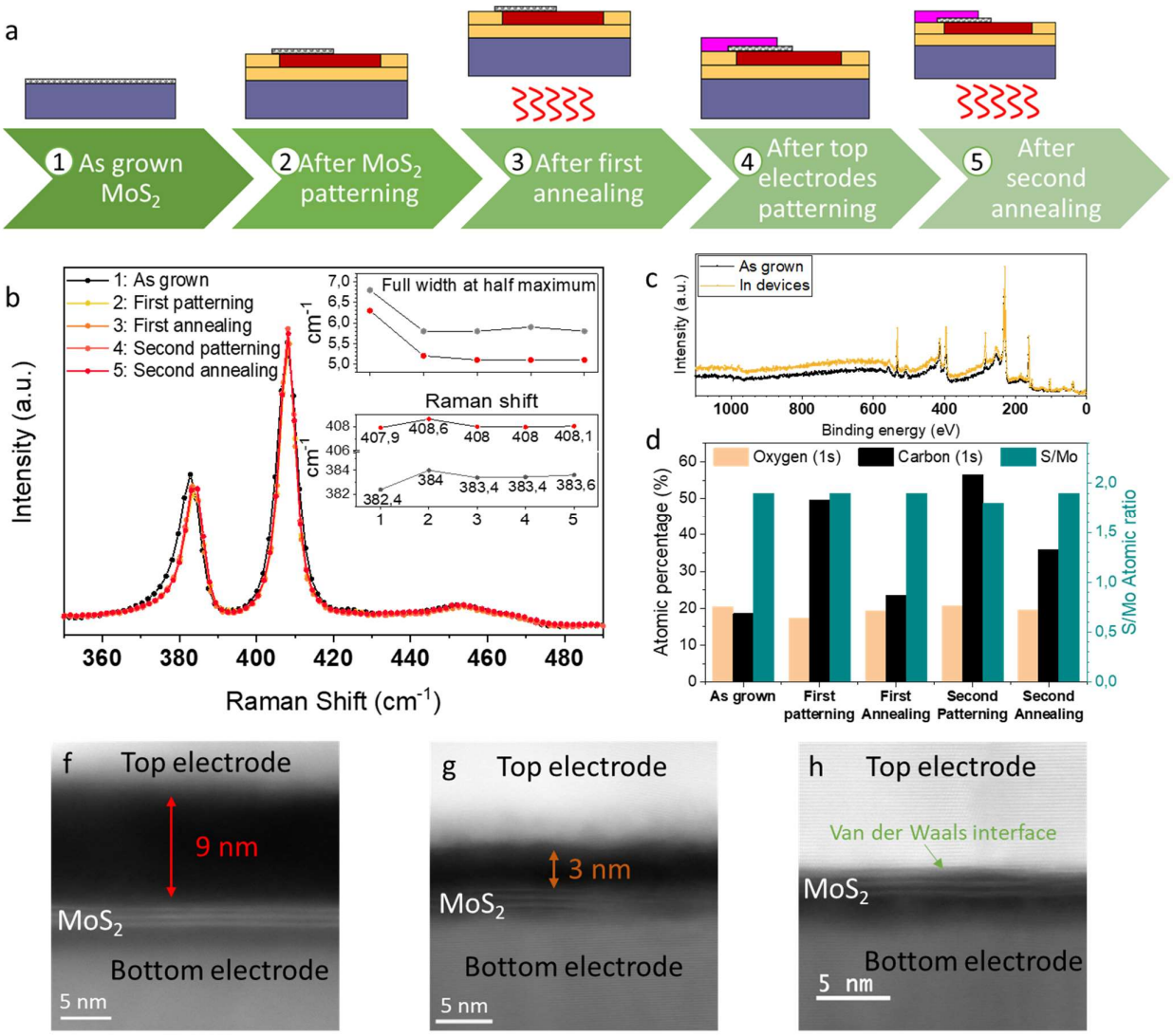

Figure 4: Study of integration process impact: Schematic of the different process steps (a). Raman spectra during the process (b), inset: evolution of E^1_{2g}, in grey, and A_{1g}, in red, peak position and full with at half maximum (FWHM). XPS spectra of MoS_2 as grown (in black) compared with MoS_2 incorporated in devices (in yellow) (c) and evolution of oxygen, carbon contents and S/Mo ratio during the process (d). Cross-section TEM image of MoS_2 integrated in the devices at the end of the process without annealing (f) with annealing (g) with transfer with Au layer (h).

3.2 Impact of the fabrication process

The processing impacts are studied on devices made with protocol I. The analyze area, visible on Figure 1-b, was characterized by Raman spectroscopy and XPS at each step described in Figure 4-a and by STEM analysis at the end of the process. The insets in Figure 4-b report the peak position and FWHM at each process step. Raman spectra exhibit almost no variation of the MoS_2 vibration peak positions and FWHM except after transfer and the first patterning. We attribute it to stress release. Actually, MoS_2 is subjected to an important thermal stress during the whole preparation process and the transfer onto another substrate allows to release the strain. The Raman analysis highlights that the MoS_2 structure is preserved during the device preparation and no structural damage is observed. The XPS analysis (Figure 4-c) shows that the S/Mo ratio and oxygen content remain constant during the process. This prove that the MoS_2 stoichiometry is preserved and the material is not oxidized during the process. On the other hand, the carbon content is increased after each lithography step and reduced by annealing. Indeed, the lithography and transfer resins bring carbon contamination onto MoS_2. This layer cannot be removed by usual methods as dipping in a basic solution or plasma treatment due to the sensitivity of MoS_2 to these processes. This observation is confirmed by TEM analysis without (Figure 4-d) and with (Figure 4-e) annealing.

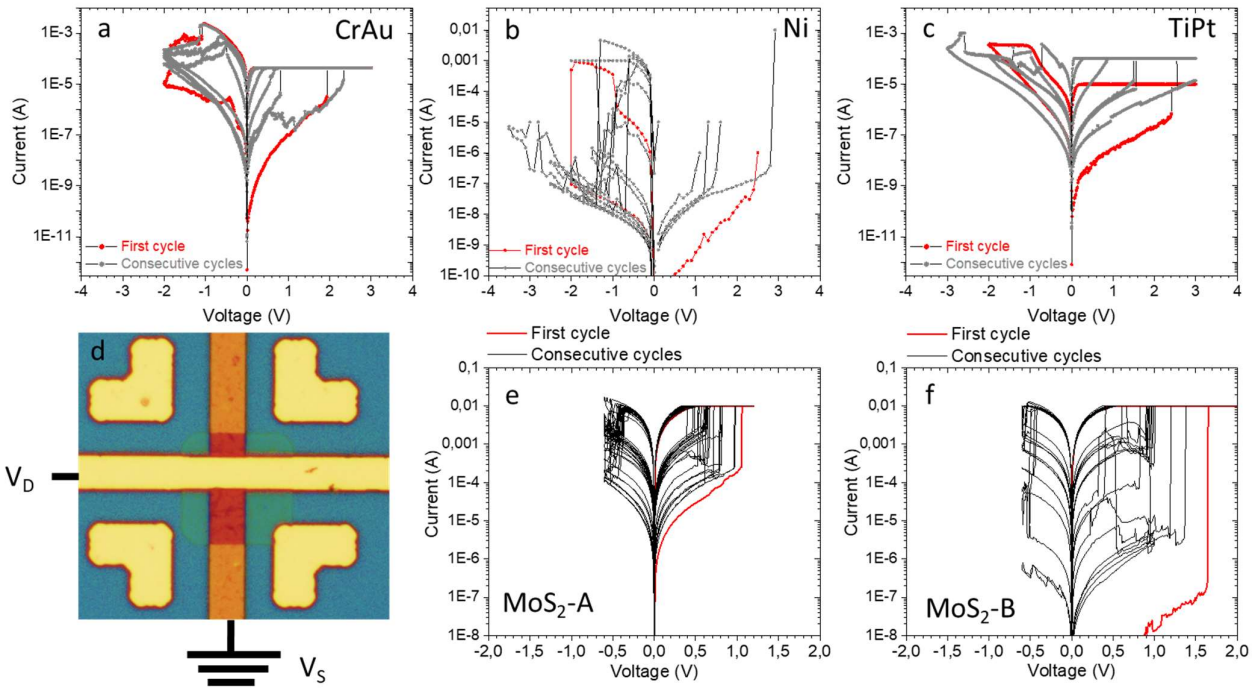

Figure 5: Electrical results: I(V) characteristic of devices made with protocol I with various metals tested as top electrodes: CrAu (a), Ni (b), TiPt (c). Geometry of the measurement set up(d). I(V) characteristics of devices made with protocol II with MoS_2-A (e) and B (f)).

A carbon contamination layer of 9 nm is observed while with annealing it is reduced to 3 nm. In protocol II, to avoid carbon contamination at the interface with the top electrode, MoS_2 was transferred with a thin layer of gold on top ensuring also a good electrical contact between MoS_2 and the top electrode. The cross section shown on Figure 4-f has been performed on a stack with Ni-via/MoS_2-A/Au. The image shows the perfect interfaces between MoS_2 and the electrodes with no carbon contamination.

To summarize, protocol I preserves the MoS_2 crystal quality and stoichiometry but introduces carbon contamination at the interface. This carbon contamination has often been reported in the literature [27], [28], [43] but its full removal has never been achieved. Protocol II allows to avoid this contamination and to obtain clean and sharp interfaces.

Electrical results

Three metals were tested as top electrodes on devices using protocol I: gold with a chromium adhesion layer, nickel and titanium layer with platinum on top for high conductivity. For this first fabrication process, only 75% of the devices were correctly patterned. In addition, switching loops were observed only for few devices probably due to carbon contamination at the MoS_2/top electrode interface. For each metal, switching loops measured on a single device are shown in figure 5a-c. A simple electrical set up was used to apply voltage sweeps and measure the current (figure 5-d). Switching loops are observed for all the devices with all three metals used as top electrodes. All the devices were initially in a resistive OFF state and successfully switched to a reversible ON state. Switching from OFF to ON is called Set, while switching from ON to OFF is called Reset. The I(V) characteristics exhibit a lack of reproducibility between devices and loops. Nevertheless, a metal-dependent behaviour, consistent with the metal ion diffusion switching mechanism [10], [44], is observed. Indeed, the current ratio between ON and OFF states (I_{ON}/I_{OFF}) is about 10^2 for CrAu and TiPt electrodes whereas it systematically reaches 10^5 for nickel electrodes. The best endurance is observed for nickel and CrAu devices for which 7 consecutive loops were observed before the devices got locked in the ON state.The same measurements were carried out on devices made with Protocol II. For these samples, 100% of the devices were correctly patterned and switching loops were observed on a larger number of devices allowing to establish a yield of "switching devices". This yield was calculated by counting the number of devices capable of performing two full switching loops as the first one could be due to a shortcut introduced during the transition from OFF to ON and a device destruction for the transition from ON to OFF. For MoS_2-A and B, the yield of switching devices is around 40%. Typical switching loops are shown in figure 5-e and f for MoS_2-A and MoS_2-B respectively. A better reproducibility is observed between devices and loops compared to devices made with protocol I. This is particularly true of MoS_2-A which shows a better reproducibility but lower current ratio than MoS_2-B. For both materials, the endurance is improved to 20 cycles. The higher

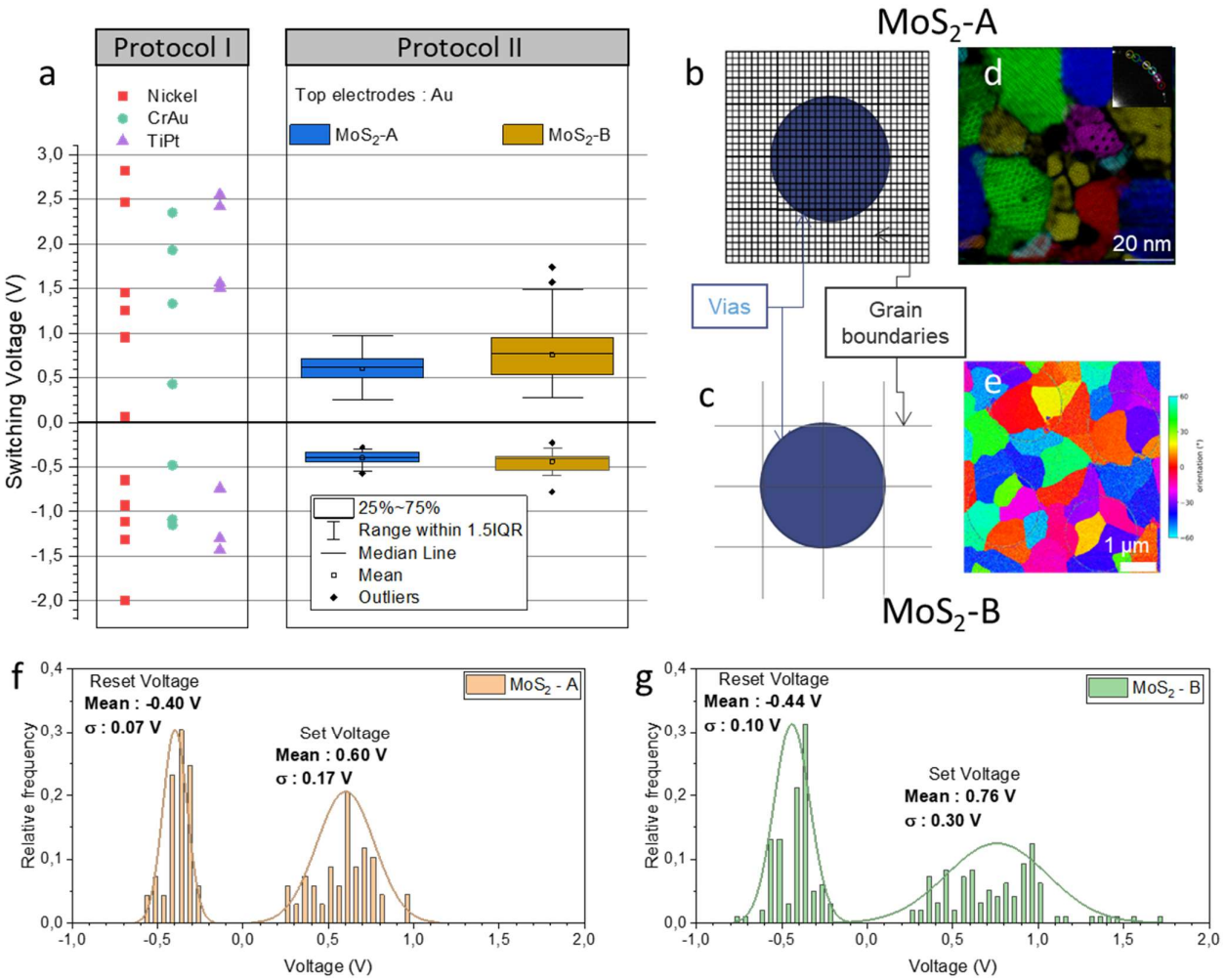

Figure 6 : (a): Statistical comparison of switching voltages for devices made with protocol I (plotted with dots) and with protocol II (plotted with boxes). These statistics were established on 8 devices and 68 data for MoS_2-A and 12 devices with 98 data for MoS_2-B. Schematics of the grain boundaries density on via for MoS_2-A (b) and B (c). Grain size illustrated by fast Fourier transform in the inset showing MoS_2 crystalline diffraction pattern and: corresponding spatial distribution of grains in false colours for MoS_2-A (d) and 4D-STEM mapping for MoS_2-B (e). Histogram and normal distribution of switching voltages for MoS_2-A (f) and B (g).

rate of switching devices, the better reproducibility between devices and the improved cyclability demonstrates the importance of the integration process quality.

By controlling the integration process, we achieve good reproducibility from one device to another. In this way, qualitative data is collected on a set of devices, enabling a detailed study of switching mechanisms, which is not possible in studies based on a single device.

Switching mechanism study

To better understand the behaviour of the devices and the switching mechanism, the switching voltages were measured and statistically analysed for each sample. They are shown in Figure 6-a. For the samples made with protocol I, the lack of data and reproducibility made impossible to draw up a clear statistics and dots were plotted for each measurement. The distribution is broad and stochastic unlike the switching voltages measured for samples made with protocol II. For the latter, the data are represented by box plots for set and reset voltages that extend over thinner areas. This confirms that optimizing the process improves the performances of the devices in terms of reproducibility and endurance. It also allows the switching voltage to be lowered thereby reducing devices power consumption. Reducing the size of the active area (from 25 µm² for protocol I to less than 1 µm in protocol I) may also have contributed to these improvements, thanks to better control of the location of the conductive filaments.

The statistical results give us the opportunity to study the switching mechanism by comparing the experimental data for MoS_2-A and B. This study is based on the work by Tang et al.[21] in which they demonstrated that the preferred location for switching is at the edge of MoS_2 nanosheets where

crystalline defects are concentrated. For our samples, the crystalline defects are concentrated at grain boundaries. The MoS_2-A grain size is in order of 10 nm while the one of MoS2-A is about 1 µm. Thus, in MoS_2-A, the density of grain boundaries is significantly higher than in MoS_2-B. This is schematized in Fig 6-b and d. As there are significantly more crystalline defects in MoS2-A, this material should switch more easily than MoS2-B., This would result in a lower energy required to form a conductive filament then a lower switching voltage with a narrow distribution. For devices containing MoS_2-B, only few grain boundaries are present on the active area (Figure 6-c) i.e. there are few sites to form conductive filaments. As a result, the switching voltage should be higher on average and with a larger distribution compared with MoS_2-A. The histograms and normal distributions of Set and Reset voltages for the two materials shown in Figure 6-d and e confirm this assumption since the average set voltage is 0.60 V for MoS_2-A compared with 0.76 V for MoS_2-B with standard deviation of 0.17 V and 0.30V respectively. Similarly, the average reset voltage is - 0.4 V and - 0.44 V for MoS_2-A and B respectively with a respective standard deviation of 0.07 V and 0.10 V. These results are consistent with the mechanisms proposed by Tang et al. about the conductive filament formation facilitated by defects in MoS2. In our case, defects are mainly located at grain boundaries and the material with higher grain boundaries density switches more easily than the one with large grains. From this result, we can conclude that defects would be benefit for vertical memory devices as they allow to obtain lower and more reproducible switching voltages.

5. Conclusion

In summary, we have developed a large-scale cleanroom integration process for MoS_2 in vertical MIM devices. We demonstrate the preservation of MoS_2 crystalline integrity, stoichiometry, and the achievement of high-quality Van der Waals interfaces by optimising the process.

Thanks to these optimisations, the yield of switching devices as well as reproducibility and performances are improved. More specifically, a ON/OFF current ratio of 10^5 is obtained, which is promising for the manufacture of RF switches in the future. By reducing the stochastic behaviour of the devices, we could study the switching mechanism. Statistics on the switching voltage and distribution of MoS_2 devices with two different grain size demonstrate that grain boundaries are the preferred location for the conductive filament formation. Therefore, the quality of MoS_2 layers, particularly the grain size, is a key factor to adjust the performances of MoS_2-based memories.

Acknowledgements

This work was supported by the French Public Authorities within the framework of the Nano2022 (IPCEI Microelectronics) project. The authors thank the “Plateforme Technologique Amont” of Grenoble, with the financial support of the CNRS Renatech network. Finally, a part of this work, carried out on the NanoCharacterization Platform (PFNC), was supported by the Recherches Technologiques de Base” Program of the French Ministry of Research.

References

[1] K. S. Novoselov *et al.*, « Electric field in atomically thin carbon films », *Science*, vol. 306, nº 5696, p. 666-669, 2004, doi: 10.1126/science.1102896.

[2] S. Lim et J. W. Suk, « Flexible temperature sensors based on two-dimensional materials for wearable devices », *Journal of Physics D: Applied Physics*, vol. 56, nº 6, 2023, doi: 10.1088/1361-6463/acaf38.

[3] L. H. Hess *et al.*, « Graphene transistor arrays for recording action potentials from electrogenic cells », *Advanced Materials*, vol. 23, nº 43, p. 5045-5049, 2011, doi: 10.1002/adma.201102990.

[4] A. Inaba, G. Yoo, Y. Takei, K. Matsumoto, et I. Shimoyama, « A graphene FET gas sensor gated by ionic liquid », présenté à Proceedings of the IEEE International Conference on Micro Electro Mechanical Systems (MEMS), 2013, p. 969-972. doi: 10.1109/MEMSYS.2013.6474408.

[5] H. Xu, J. Wu, Q. Feng, N. Mao, C. Wang, et J. Zhang, « High responsivity and gate tunable graphene-MoS2 hybrid phototransistor », *Small*, vol. 10, nº 11, p. 2300-2306, 2014, doi: 10.1002/smll.201303670.

[6] M. M. Rehman, H. M. M. U. Rehman, J. Z. Gul, W. Y. Kim, K. S. Karimov, et N. Ahmed, « Decade of 2D-materials-based RRAM devices: a review », *Science and Technology of Advanced Materials*, vol. 21, nº 1, p. 147-186, 2020, doi: 10.1080/14686996.2020.1730236.

[7] R. Ge *et al.*, « Atomristor: Nonvolatile Resistance Switching in Atomic Sheets of Transition Metal Dichalcogenides », *Nano Lett.*, vol. 18, nº 1, p. 434-441, janv. 2018, doi: 10.1021/acs.nanolett.7b04342.

[8] M. Kim *et al.*, « Monolayer molybdenum disulfide switches for 6G communication systems », *Nat Electron*, vol. 5, nº 6, Art. nº 6, juin 2022, doi: 10.1038/s41928-022-00766-2.

[9] M. Kim, E. Pallecchi, H. Happy, et D. Akinwande, « Single-Pole-Double-Throw RF switches based on monolayer MoS2 », in *2021 Device Research Conference (DRC)*, juin 2021, p. 1-2. doi: 10.1109/DRC52342.2021.9467136.

[10] R. Ge *et al.*, « A Library of Atomically Thin 2D Materials Featuring the Conductive-Point Resistive Switching Phenomenon », *Advanced Materials*, vol. 33, nº 7, p. 2007792, 2021, doi: 10.1002/adma.202007792.

[11] K. P. O’Brien *et al.*, « Advancing 2D Monolayer CMOS Through Contact, Channel and Interface Engineering », in *2021 IEEE International Electron Devices Meeting (IEDM)*, déc. 2021, p. 7.1.1-7.1.4. doi: 10.1109/IEDM19574.2021.9720651.

[12] C. J. Dorow *et al.*, « Gate length scaling beyond Si: Mono-layer 2D Channel FETs Robust to Short Channel Effects », in *2022 International Electron Devices Meeting (IEDM)*, San

Francisco, CA, USA: IEEE, déc. 2022, p. 7.5.1-7.5.4. doi: 10.1109/IEDM45625.2022.10019524.
[13] D. Kim *et al.*, « Emerging memory electronics for non-volatile radiofrequency switching technologies », *Nat Rev Electr Eng*, vol. 1, nº 1, Art. nº 1, janv. 2024, doi: 10.1038/s44287-023-00001-w.
[14] M. Naqi *et al.*, « Multilevel artificial electronic synaptic device of direct grown robust MoS2 based memristor array for in-memory deep neural network », *npj 2D Mater Appl*, vol. 6, nº 1, p. 53, août 2022, doi: 10.1038/s41699-022-00325-5.
[15] G. Molas et E. Nowak, « Advances in Emerging Memory Technologies: From Data Storage to Artificial Intelligence », *Applied Sciences*, vol. 11, nº 23, Art. nº 23, janv. 2021, doi: 10.3390/app112311254.
[16] N. Wainstein, G. Adam, E. Yalon, et S. Kvatinsky, « Radiofrequency Switches Based on Emerging Resistive Memory Technologies - A Survey », *Proceedings of the IEEE*, vol. 109, nº 1, p. 77-95, janv. 2021, doi: 10.1109/JPROC.2020.3011953.
[17] M. Wang *et al.*, « Robust memristors based on layered two-dimensional materials », *Nat Electron*, vol. 1, nº 2, Art. nº 2, févr. 2018, doi: 10.1038/s41928-018-0021-4.
[18] Z. Yin, Z. Zeng, J. Liu, Q. He, P. Chen, et H. Zhang, « Memory Devices Using a Mixture of MoS2 and Graphene Oxide as the Active Layer », *Small*, vol. 9, nº 5, p. 727-731, 2013, doi: 10.1002/smll.201201940.
[19] S. Bhattacharjee *et al.*, « Insights into Multilevel Resistive Switching in Monolayer MoS $_2$ », *ACS Appl. Mater. Interfaces*, vol. 12, nº 5, p. 6022-6029, févr. 2020, doi: 10.1021/acsami.9b15677.
[20] S. Wang *et al.*, « All-atomristor logic gates », *Nano Res.*, oct. 2022, doi: 10.1007/s12274-022-5042-7.
[21] B. Tang *et al.*, « Wafer-scale solution-processed 2D material analog resistive memory array for memory-based computing », *Nat Commun*, vol. 13, nº 1, p. 3037, déc. 2022, doi: 10.1038/s41467-022-30519-w.
[22] F. Zhang *et al.*, « Electric-field induced structural transition in vertical MoTe2- and Mo1–xWxTe2-based resistive memories », *Nature Mater*, vol. 18, nº 1, Art. nº 1, janv. 2019, doi: 10.1038/s41563-018-0234-y.
[23] X. Wu *et al.*, « Electron irradiation-induced defects for reliability improvement in monolayer MoS2-based conductive-point memory devices », *npj 2D Mater Appl*, vol. 6, nº 1, Art. nº 1, mai 2022, doi: 10.1038/s41699-022-00306-8.
[24] B. Hyot *et al.*, « Towards large scale integration of MoS2/graphene heterostructure with ALD-grown MoS2 », *Nanotechnology*, 2024, doi: 10.1088/1361-6528/ad1d7c.
[25] M. L. Verma, Sukriti, B. S. Dhanya, R. Saini, A. Das, et R. S. Varma, « Synthesis and application of graphene-based sensors in biology: a review », *Environ Chem Lett*, vol. 20, nº 3, p. 2189-2212, juin 2022, doi: 10.1007/s10311-022-01404-1.
[26] M. C. Lemme, D. Akinwande, C. Huyghebaert, et C. Stampfer, « 2D materials for future heterogeneous electronics », *Nat Commun*, vol. 13, nº 1, Art. nº 1, mars 2022, doi: 10.1038/s41467-022-29001-4.
[27] Y.-C. Lin, C.-C. Lu, C.-H. Yeh, C. Jin, K. Suenaga, et P.-W. Chiu, « Graphene Annealing: How Clean Can It Be? », *Nano Lett.*, vol. 12, nº 1, p. 414-419, janv. 2012, doi: 10.1021/nl203733r.
[28] R. Tilmann *et al.*, « Identification of Ubiquitously Present Polymeric Adlayers on 2D Transition Metal Dichalcogenides », *ACS Nano*, p. acsnano.3c01649, mai 2023, doi: 10.1021/acsnano.3c01649.
[29] Y. Liu *et al.*, « Approaching the Schottky-Mott limit in van der Waals metal-semiconductor junctions /639/301/1005/1007 /639/166/987 /639/925/357/1018 /639/925/927/1007 /120 /128 /140/133 /142 /142/126 /144 letter », *Nature*, vol. 557, nº 7707, p. 696-700, 2018, doi: 10.1038/s41586-018-0129-8.
[30] Y. Wang et M. Chhowalla, « Making clean electrical contacts on 2D transition metal dichalcogenides », *Nat Rev Phys*, vol. 4, nº 2, Art. nº 2, févr. 2022, doi: 10.1038/s42254-021-00389-0.
[31] C. Zhang *et al.*, « Systematic study of electronic structure and band alignment of monolayer transition metal dichalcogenides in Van der Waals heterostructures », *2D Mater.*, vol. 4, nº 1, p. 015026, nov. 2016, doi: 10.1088/2053-1583/4/1/015026.
[32] S. Das, H.-Y. Chen, A. V. Penumatcha, et J. Appenzeller, « High performance multilayer MoS2 transistors with scandium contacts », *Nano Letters*, vol. 13, nº 1, p. 100-105, 2013, doi: 10.1021/nl303583v.
[33] S. Cadot *et al.*, « A novel 2-step ALD route to ultra-thin MoS2 films on SiO2 through a surface organometallic intermediate », *Nanoscale*, vol. 9, nº 2, p. 538-546, janv. 2017, doi: 10.1039/c6nr06021h.
[34] « 2'' wafer CVD monolayers or few-layers », 2D Semiconductors. Consulté le: 5 juillet 2023. [En ligne]. Disponible sur: https://www.2dsemiconductors.com/2inch-wafer-cvd-monolayers/
[35] S. Mignuzzi *et al.*, « Effect of disorder on Raman scattering of single-layer Mo S 2 », *Phys. Rev. B*, vol. 91, nº 19, p. 195411, mai 2015, doi: 10.1103/PhysRevB.91.195411.
[36] A. M. Stacy et D. T. Hodul, « Raman spectra of IVB and VIB transition metal disulfides using laser energies near the absorption edges », *Journal of Physics and Chemistry of Solids*, vol. 46, nº 4, p. 405-409, janv. 1985, doi: 10.1016/0022-3697(85)90103-9.
[37] H. Li *et al.*, « From Bulk to Monolayer MoS2: Evolution of Raman Scattering », *Advanced Functional Materials*, vol. 22, nº 7, p. 1385-1390, 2012, doi: 10.1002/adfm.201102111.
[38] A. M. de Jong *et al.*, « Sulfidation mechanism by molybdenum catalysts supported on silica/silicon(100) model support studied by surface spectroscopy », *J. Phys. Chem.*, vol. 97, nº 24, p. 6477-6483, juin 1993, doi: 10.1021/j100126a024.
[39] J. C. Muijsers, T. Weber, R. M. Vanhardeveld, H. W. Zandbergen, et J. W. Niemantsverdriet, « Sulfidation Study of Molybdenum Oxide Using MoO3/SiO2/Si(100) Model Catalysts and Mo-IV3-Sulfur Cluster Compounds », *Journal of Catalysis*, vol. 157, nº 2, p. 698-705, déc. 1995, doi: 10.1006/jcat.1995.1335.
[40] E. Nolot, S. Cadot, F. Martin, P. Hönicke, C. Zech, et B. Beckhoff, « In-line characterization of ultrathin transition metal dichalcogenides using X-ray fluorescence and X-ray photoelectron spectroscopy », *Spectrochimica Acta - Part B Atomic Spectroscopy*, vol. 166, 2020, doi: 10.1016/j.sab.2020.105788.
[41] Th. Weber, J. C. Muijsers, J. H. M. C. van Wolput, C. P. J. Verhagen, et J. W. Niemantsverdriet, « Basic Reaction Steps in the Sulfidation of Crystalline MoO $_3$ to MoS $_2$, As Studied by X-ray Photoelectron and Infrared Emission Spectroscopy », *J. Phys. Chem.*, vol. 100, nº 33, p. 14144-14150, janv. 1996, doi: 10.1021/jp961204y.
[42] D. Dosenovic *et al.*, « Mapping domain junctions using 4D-STEM: toward controlled properties of epitaxially grown

transition metal dichalcogenide monolayers », *2D Mater.*, 2023, doi: 10.1088/2053-1583/acf3f9.
[43] B. R. Borodin, F. A. Benimetskiy, V. Yu. Davydov, I. A. Eliseyev, et P. A. Alekseev, « Effect of Interfacial Contamination on the Charge Redistribution and Photoluminescence of the MoSe2/Au Heterostructure: Implications for Photodevices », *ACS Appl. Nano Mater.*, juill. 2023, doi: 10.1021/acsanm.3c01883.
[44] R. Ge *et al.*, « Atomristors: Memory Effect in Atomically-thin Sheets and Record RF Switches », in *2018 IEEE International Electron Devices Meeting (IEDM)*, déc. 2018, p. 22.6.1-22.6.4. doi: 10.1109/IEDM.2018.8614602.